Asian Journal of Chemistry; Vol. 36, No. 7 (2024), 1657-1671

ASIAN JOURNAL OF CHEMISTRY

https://doi.org/10.14233/ajchem.2024.31926

Photocatalytic and Conductivity Studies of Proton Exchanged Defect Pyrochlore, $KMn_{0.33}Te_{1.67}O_6$ and its Application in Pb^{2+} Removal

ASHA SIDDIKHA[1], MUGA VITHAL[2,*] and BOODIDA SATHYANARAYANA[1]

[1]Department of Chemistry, JNTUH University College of Engineering, Science and Technology, Hyderabad-500085, India
[2]Department of Chemistry, Osmania University, Hyderabad-500007, India

*Corresponding author: E-mail: mugavithal@gmail.com; muga_vithal@osmania.ac.in

Received: 10 May 2024; *Accepted*: 14 June 2024; *Published online*: 29 June 2024; AJC-21686

Ion-conducting oxide materials have incredible technological importance, particularly in devices such as sensors, fuel cells and steam electrolysis cells. In this work, a new proton exchanged defect pyrochlore, $HMn_{0.33}Te_{1.67}O_6$ (HMnTeO), was synthesized by ion-exchange method at room temperature by dissolving $KMn_{0.33}Te_{1.67}O_6$ (KMnTeO) in 5 M HCl solution for 48 h. It was thoroughly characterized by powder-XRD, FESEM-EDX, TEM-HRTEM, FT-IR, Raman, TGA, UV-Vis DRS, PL and XPS techniques. The photocatalytic and DC conductivity of HMnTeO were compared with parent KMnTeO material. The protonated form (HMnTeO) exhibits higher photocatalytic activity against methylene blue degradation and superior DC conductivity compared to parent KMnTeO. The participation of radical species in dye degradation was investigated through scavenger and terephthalic experiments. Based on the results obtained, a probable mechanism was also proposed. Removal of Pb^{2+} ions from aqueous $Pb(NO_3)_2$ was also accomplished using parent KMnTeO.

Keywords: Defect pyrochlore, HMnTeO, Optical properties, Methylene blue, Lead(II), DC conductivity.

INTRODUCTION

Water consumption across the globe has increased by about 5-10 times during the last few decades due to the phenomenal industrial growth and an increase in population. It was observed that 80% of the wastewater from industries and domestic activities was discharged without proper treatment into the environment causing heavy damage to (i) aquatic, terrestrial plants and animals and (ii) ecological balance. Many organic pollutants (including pharmaceuticals) in water are non-biodegradable and prevent the penetration of sunlight into waterbodies, inhibiting the photosynthesis cycle of aquatic plants [1,2]. Thus, wastewater treatment is one of the top-rated global issues. The wastewater generated by industry and human domestic activities contains harmful chemicals, such as organic dyes, medicines, pesticides and organic byproducts. These substances are toxic to both aquatic and terrestrial plants and animals, leading to their extermination. A significant proportion of organic dyes and pharmaceuticals consist of aromatic rings, which possess high toxicity and present challenges in terms of decomposition. Consequently, they are recognized as a significant contributor to ecological disruption. Additionally, eliminating heavy metal ions from aqueous solutions is essential in water pollution control [3,4]. The presence of Pb^{2+} in industrial effluent is particularly hazardous to the aquatic ecosystem and can potentially cause health hazards to humans. Thus, it is imperative to remove Pb^{2+} from wastewater for the sake of the environment and human health. Hence, the process of treating wastewater is essential for the survival of both plant and animal species. Although traditional physical, chemical and biological methods for treating wastewater are now common, however, due to the high costs, generation of additional contaminants and necessitate complex equipment. Advanced oxidation processes (AOPs) are effective for treating wastewater with stubborn pollutants because they utilize highly reactive substances like free radicals ($^{\bullet}OH$, $O_2^{\bullet-}$ and peroxide), as well as holes and electrons. Photocatalysis, a type of advanced oxidation process (AOP) that uses inorganic semiconductors, is commonly used for environmental remediation due to its chemical stability. It entails the use of very small instruments, which are cost-effective, and results in the creation of harmless byproducts [4-6].

Pyrochlore, a naturally occurring mineral of composition $(Na,Ca)_2Nb_2O_6(OH,F)$, is a common oxide text book structure

This is an open access journal, and articles are distributed under the terms of the Attribution 4.0 International (CC BY 4.0) License. This license lets others distribute, remix, tweak, and build upon your work, even commercially, as long as they credit the author for the original creation. You must give appropriate credit, provide a link to the license, and indicate if changes were made.

with potential applications in various fields. It is abbreviated as $A_2B_2O_6O'$ (ideal pyrochlore). It crystallizes in cubic lattice with space group *Fd*3*m*. An perfect pyrochlore is characterized by the arrangement of BO_6 octahedral units that share corners and zig-zag A_2O' chains. The zig-zag A_2O' chains are penetrating the BO_6 units, resulting in a 3D framework structure with vast tunnels.The A cations have a greater size and a coordination number of 8, whereas the B cations have a smaller size and a coordination number of 6. The radius ratio limit for A and B cations in an ideal pyrochlore is between 1.93 and 2.75, however the exact limitations are not well-documented. The weak attractive contact between BO_6 octahedral units and A_2O' chains results in the formation of deficient compositions, such as $A_2B_2O_6$ (lacking atom O′) and AB_2O_6 (lacking atoms A and O′), which are often known as defect pyrochlore or β-pyrochlore. Pyrochlore with defects also forms cubic lattices exhibiting the same space group. The typical combinations of A and B cations are (A^{3+}, B^{4+}), (A^{2+}, B^{5+}) and (A^{+}, B^{6+}) [7-10]. Therefore, the pyrochlore structure is flexible and may be modified by replacing different valence cations, allowing for the adjustment of its properties.

Extensive studies have been conducted on materials within the defect pyrochlore family of type AB_2O_6 (or $ABB'O_6$), specifically those containing hexavalent tungsten or hexavalent molybdenum at the B site. Nevertheless, there is a limited amount of research available on hexavalent tellurium (at B site) pyrochlore, with only a few investigations conducted [11-15]. Recently, we attempted to prepare defect pyrochlore for the composition of $KMn_{0.33}Te_{1.67}O_6$ and its photocatalytic activity was examined by combining it with *g*-C_3N_4 [16]. The protonated form of $KMn_{0.33}Te_{1.67}O_6$ was obtained by stirring it in HCl solution for 48 h and its photocatalytic activity and DC conductivity are presented. The results obtained are also compared with parent $KMn_{0.33}Te_{1.67}O_6$.

EXPERIMENTAL

Chemicals such as potassium nitrate (KNO_3, SDFCL, 99%), manganese acetate tetrahydrate ($Mn(CH_3COO)_2{\cdot}4H_2O$, SDFCL, 99%), telluric acid ($Te(OH)_6$, Sigma Aldrich, 99%), nitric acid (HNO_3, SDFCL, 98%) and acetone (C_3H_6O, SDFCL, 98%) were used without any purification. For photocatalytic degradation studies, methylene blue (Fluka, 98.5%); *p*-benzoquinone (Sigma Aldrich, 98%), isopropyl alcohol (SDFCL, 98%) and ammonium oxalate (Ranbaxy, 99%) and terephthalic acid (Finar, 99.9%) were also used. Double distilled water was used for all experimental work.

Preparation of catalysts

Preparation of $KMn_{0.33}Te_{1.67}O_6$ (KMnTeO): The title compound was prepared using the standard high temperature solid-state method. Analytical grade KNO_3, $Mn(CH_3COO)_2{\cdot}4H_2O$ and $Te(OH)_6$ were employed as starting materials. Calculated quantities of the reactants for 2 g of final product were weighed and thoroughly crushed in an agate mortar using acetone. The well-ground mixture was sequentially heated at 300 ºC (6 h) and 600 °C (24 h) with one intermittent grinding. A light black-coloured compound was obtained.

Preparation of $HMn_{0.33}Te_{1.67}O_6$ (HMnTeO): The proton-exchange product was prepared using an ion-exchange method. About 0.5 g of solid KMnTeO was added to 100 mL of 5 M HCl solution and stirred for 48 h at ambient temperature. The contents were separated, washed with double distilled water several times and finally dried at 60 ºC (product-1). The supernatant solution was slowly heated to dryness and this solid was named as product-2. Both product-1 and product-2 were subjected to powder XRD measurements for phase confirmation.

Characterization: The powder X-ray powder diffraction (XRD) patterns were recorded using a Rigaku Miniflex 600 X-ray diffractometer with Cu-*K*α radiation (λ = 1.5406 Å) at 40 kV and 15 mA. They were collected at 2θ angles of 10-80º with 0.02° per step. The structural characterization was then done by carrying out a Rietveld refinement analysis of the XRD data using Fullprof suit. Field emission scanning electron microscopy (FESEM) images and energy dispersive X-ray spectrum (EDX) were performed with a Carl Zeiss model Ultra 55 equipped with Oxford instruments X-MaxN SDD system operated with INCA software. Transmission electron microscopy (TEM)-high-resolution TEM (HRTEM) was carried out on a Jeol JEM-2100F at an accelerating voltage of 200 kV. Fourier transform infrared spectra were recorded on a Perkin-Elmer Spectrum One FT-IR spectrophotometer over the 1200-400 cm^{-1} wavelength range using KBr pallet. Raman scattering spectra were obtained using a Wi-Tec alpha 300 AR laser confocal microscopes (T-LCM) with an Ar excitation wavelength of 532 nm. Thermogravimetric (TGA) analysis was performed with a Perkin-Elmer STA 6000 with a heating rate of 10 ºC/min under the N_2 stream with a temperature ranging from 30 to 900 ºC. The UV-Vis diffuse reflectance absorption spectra were performed over the 200-800 nm wavelength range by a JASCO V650 UV/Vis spectrophotometer, with $BaSO_4$ as a reference. Photoluminescence (PL) emission spectra were recorded using a Shimadzu RF-5300PC system with laser excitation at 240 nm. The X-ray photoelectron spectroscopy (XPS) was performed with a Quantum 2000 Scanning ESCA Microprobe using a monochromatic Al-*K*α X-ray source. The C 1s signal was set to 284.8 eV for charge correction of the obtained XPS spectra.

Ion-exchange experiment for the removal of Pb^{2+}: In brief, 0.5 g of KMnTeO was added to 50 mL of $Pb(NO_3)_2$ solution (0.011 M) under constant stirring for 24 h. The experiment was conducted at room temperature and a pH of 1.0 and 5.0. Subsequently, the supernatant liquid was separated by centrifugation to extract the solid KPbMnTeO from the solution. Both supernatant liquid and solid were examined for ion analysis.

Photocatalytic studies: The photocatalytic performance of all the prepared photocatalysts was determined by monitoring the degradation of the methylene blue dye with visible light irradiation. The Heber scientific (HVAR-MP400 model) annular-type photoreactor was used for the photocatalytic studies. A blank experiment was carried by irradiating the methylene blue solution without incorporating the photocatalyst. At first, a certain amount of photocatalyst (50 mg) and methylene blue solution (2×10^{-5} M; 50 mL) were dispersed in a long glass tube. The mixed solution was then continuously bubbled with atmospheric air to distribute the catalyst particles through

the solution uniformly. Before irradiation, the photocatalyst suspensions containing methylene blue solution were allowed to reach the adsorption–desorption equilibrium for 60 min in the dark. Then, the suspension was irradiated with a 300 W tungsten lamp as visible light source, which was placed inside the photoreactor setup. All the reaction processes were conducted in the presence of oxygen, supplied by air bubbling. A sample of 3 mL solution was taken for every 30 min during the irradiation, which was centrifuged to remove photocatalyst particles. The concentration of methylene blue was determined by the change in the optical absorbance at 662 nm (JASCO V650 UV/Vis spectrophotometer), which corresponded to the wavelength with maximum optical absorption for methylene blue. The whole photocatalytic degradation experiment lasted for 180 min. In addition, the stability of catalyst on photocatalytic methylene blue degradation was investigated by carrying out repeated photocatalytic tests for five cycles. To accomplish this, a fixed quantity of catalyst (50 mg) was taken in 50 mL of 2×10^{-5} M methylene blue solution and the photocatalytic degradation studies were performed using the same procedure described in the above process.

Detection of reactive species: Radical trapping experiments were performed to inspect the role of reactive species in the photocatalytic degradation of methylene blue with the HMnTeO. Three different types of scavengers were preferred for this purpose for example, ammonium oxalate (as scavenger of h^+), isopropyl alcohol (as scavenger of $^{\bullet}OH$) and *p*-benzoquinone (as scavenger of $O_2^{\bullet-}$). Typically, 2 mL of each scavenger (2 mM) was dispersed in reaction solutions consisting of the same amount of catalyst and methylene blue solution and the mixed solution was exposed to visible light for 180 min.

Terephthalic acid can be used as a molecular probe to monitor the generated hydroxyl radicals during photocatalysis. The reaction product of terephthalic acid and $^{\bullet}OH$ radicals is 2-hydroxyterephthalic acid (HTA), which emits a fluorescence at 425 nm. A 50 mg of sample was added to terephthalic acid solution (50 mL, 0.03 mmol L^{-1}) in 2 mmol L^{-1} NaOH. The fluorescence emission peak intensity of HTA was recorded on the photoluminescence spectrometer at an excitation wavelength of 325 nm [17].

Conductivity studies: A two-probe method was employed to measure the DC conductivity of KMnTeO and HMnTeO in the temperature range 320-650 K. The samples were pressed in the form of pellets 10 mm in diameter coated with silver paint for electrical contact and sintered at an appropriate temperature. The current was measured using Keithley electrometer 6485C. The pellet dimensions and the resistance (calculated from the current measured and voltage applied) were used to obtain the conductivity (σ_{dc}) value.

RESULTS AND DISCUSSION

Parent $KMn_{0.33}Te_{1.67}O_6$ (KMnTeO) was prepared by the standard high-temperature solid-state method. The protonated form of KMnTeO was obtained using ion-exchange method. Defect pyrochlores of type AB_2O_6 (or $AB_{2-x}B'_xO_6$) are known to give ion exchanged products by stirring them in a solution of guest ions [15,18,19]. In present investigation, KMnTeO was stirred in 5 M HCl solution for 48 h and the probable reaction is:

$$KMn_{0.33}Te_{1.67}O_6(\text{solid}) + HCl\ (\text{solution}) \xrightarrow{\text{Stir/48 h}} K_{1-x}H_xMn_{0.33}Te_{1.67}O_6(\text{solid}) + KCl\ (\text{solution})$$

XRD studies: The powder XRD pattern of product-2 gave *d*-lines at 2θ of 28.50º, 40.70º, 50.50º, 58.98º and 66.76º (Fig. 1). These values correspond to KCl (JCPDS card No. 89-3619). The XRD patterns of product-1 *i.e.* $K_{1-x}H_xMn_{0.33}Te_{1.67}O_6$ (HMnTeO) is similar to that of parent KMnTeO without any impurity lines (Fig. 2a). Nevertheless, when plotted in an expanded scale, a finite shift in the position of 2θ towards a higher angle is observed (Fig. 2b). This shift is attributed to a change in the ionic radius of H^+ (0.037 nm for eight coordination) and K^+ (0.133 nm for eight coordination). The similarity of XRD patterns of KMnTeO and HMnTeO shows that the parent lattice is unchanged upon ion-exchange. Thus, HMnTeO also crystallized in a cubic lattice and the *d*-values of HMnTeO are least square fitted using POWD software to deduce the cell parameters. It is observed that HMnTeO also crystallized in a cubic lattice with defect pyrochlore structure (space group $Fd\bar{3}m$) and Z = 8 [20]. The lattice parameter (a) was found to be 10.076 Å, which is higher than that of parent KMnTeO (a = 10.034 Å). As the ionic radius of H^+ is lower than K^+, replacing K^+ by H^+ is expected to shrink the unit cell. However, the observed increase of lattice parameter indicates that instead of H^+, H_3O^+ species might have entered into the KMnTeO lattice.

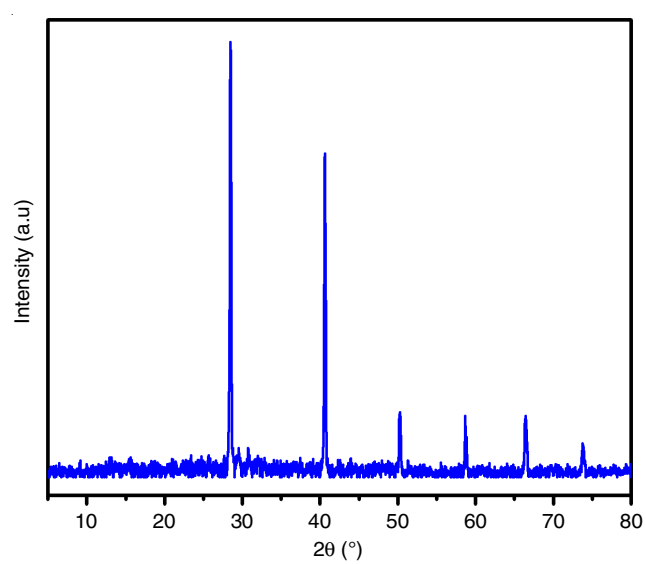

Fig. 1. Powder XRD spectrum of KCl

FESEM-EDS studies: Figs. 3a and 3c show the relevant FESEM images for parent KMnTeO and HMnTeO samples, respectively. Both samples exhibit a similar morphology characterized by the aggregates with different sizes and polyhedral shapes. The aggregation of the particles is attributed to the solid state reaction at very high temperatures. No specific morphology change was observed due to the incorporation of H_3O^+ ions. The EDX results of the samples are shown in Figs. 3b and 3d. The peaks corresponding to the elements Mn, Te and O were

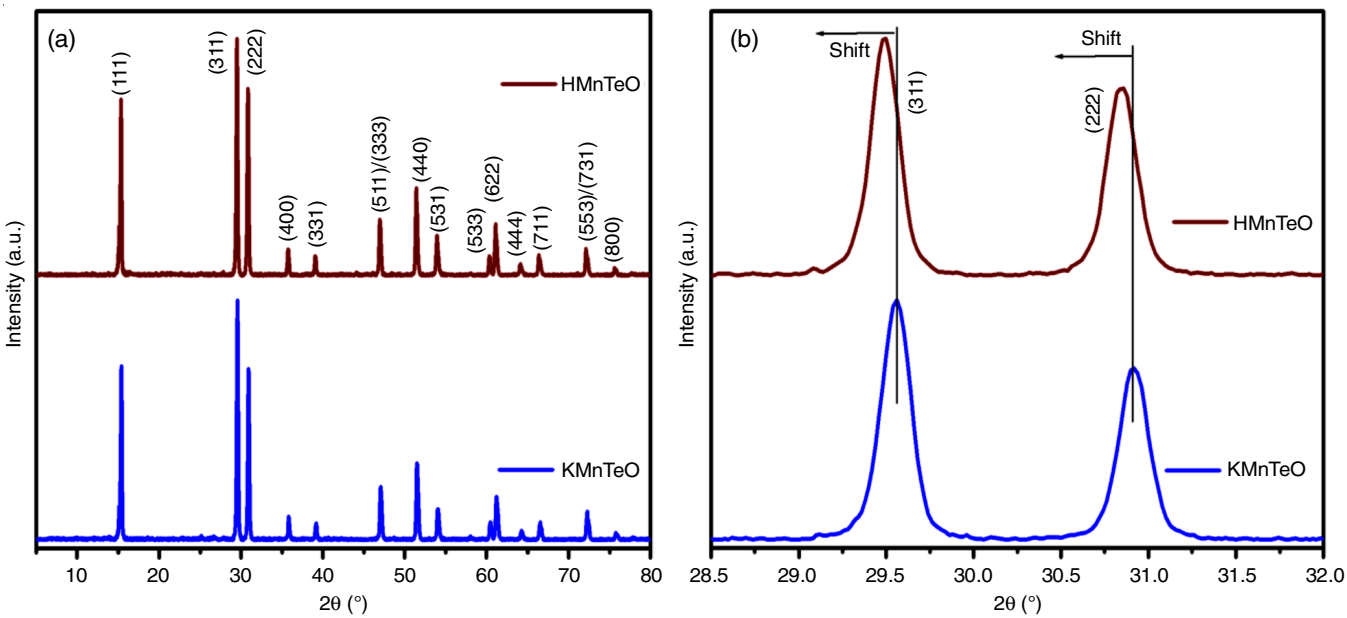

Fig. 2. (a) Powder XRD patterns of KMnTeO and HMnTeO, (b) Enlarged view of selected 2θ (28.5-32°) region

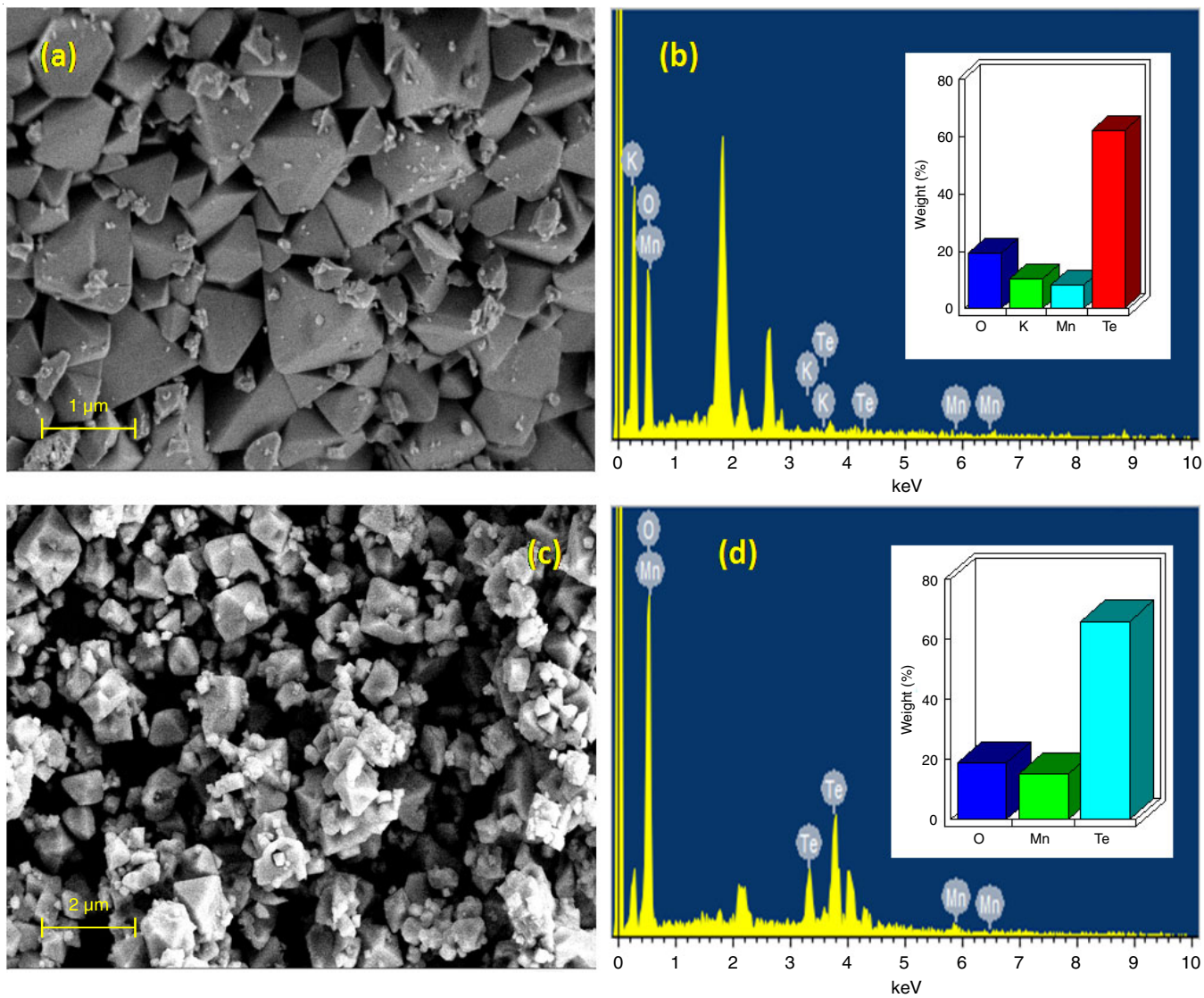

Fig. 3. (a,c) FESEM images and (b,d) EDX profiles of KMnTeO and HMnTeO (inset shows the elemental composition in wt.%)

observed in both samples. Additionally, the EDX spectrum for the HMnTeO shows no peaks associated with potassium, suggesting the complete exchange of potassium by protonic species. However, the hydrogen element was not found in the EDX spectrum of HMnTeO since it is lightweight. The weight and atomic percentage of elements analyzed by EDX are shown in Table-1. The analysis of EDX mapping was also applied to KMnTeO and HMnTeO, which confirmed the presence and homogenously distributed K, Mn, Te and O elements on the surface of the samples (Fig. 4). These results suggested that the prepared samples were devoid of any impurities.

TEM studies: Further insights into the size, morphology and crystalline properties of KMnTeO and HMnTeO samples were obtained from TEM and HRTEM analysis. The TEM images (Fig. 5) of KMnTeO and HMnTeO revealed irregularly shaped particles with an average particle size of 30-50 nm and some degree of particle agglomeration (Figs. 5a and c). The HRTEM results clearly justify the high crystalline nature of both samples (Figs. 5b and d). The calculated interplanar spacing of adjacent lattice fringes of parent KMnTeO is 0.581 nm and 0.583 nm, which matches the (111) plane of the cubic phase of KMnTeO. It can be seen that the interplanar spacing of HMnTeO (0.586

TABLE-1
THE ELEMENTAL COMPOSITION OF KMnTeO AND HMnTeO

Catalyst	Elemental composition (wt.%)					Elemental composition (at.%)				
	K	Mn	Te	O	H	K	Mn	Te	O	H
KMnTeO	10.32	8.24	62.07	19.37	–	12.50	7.11	23.04	57.35	–
HMnTeO	–	15.20	66.05	18.75	–	–	14.07	26.33	59.60	–

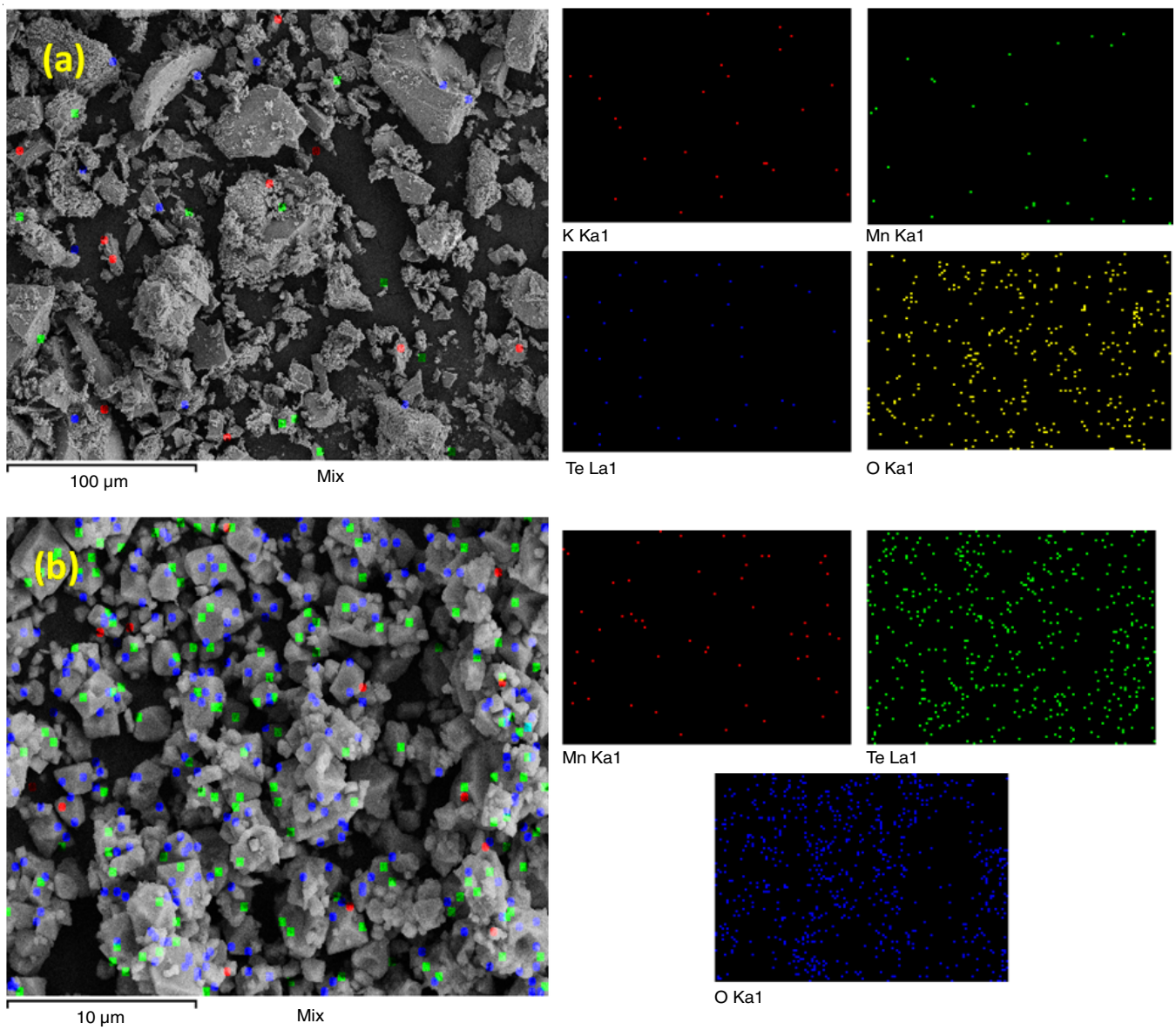

Fig. 4. EDX elemental mapping images of (a) KMnTeO and (b) HMnTeO

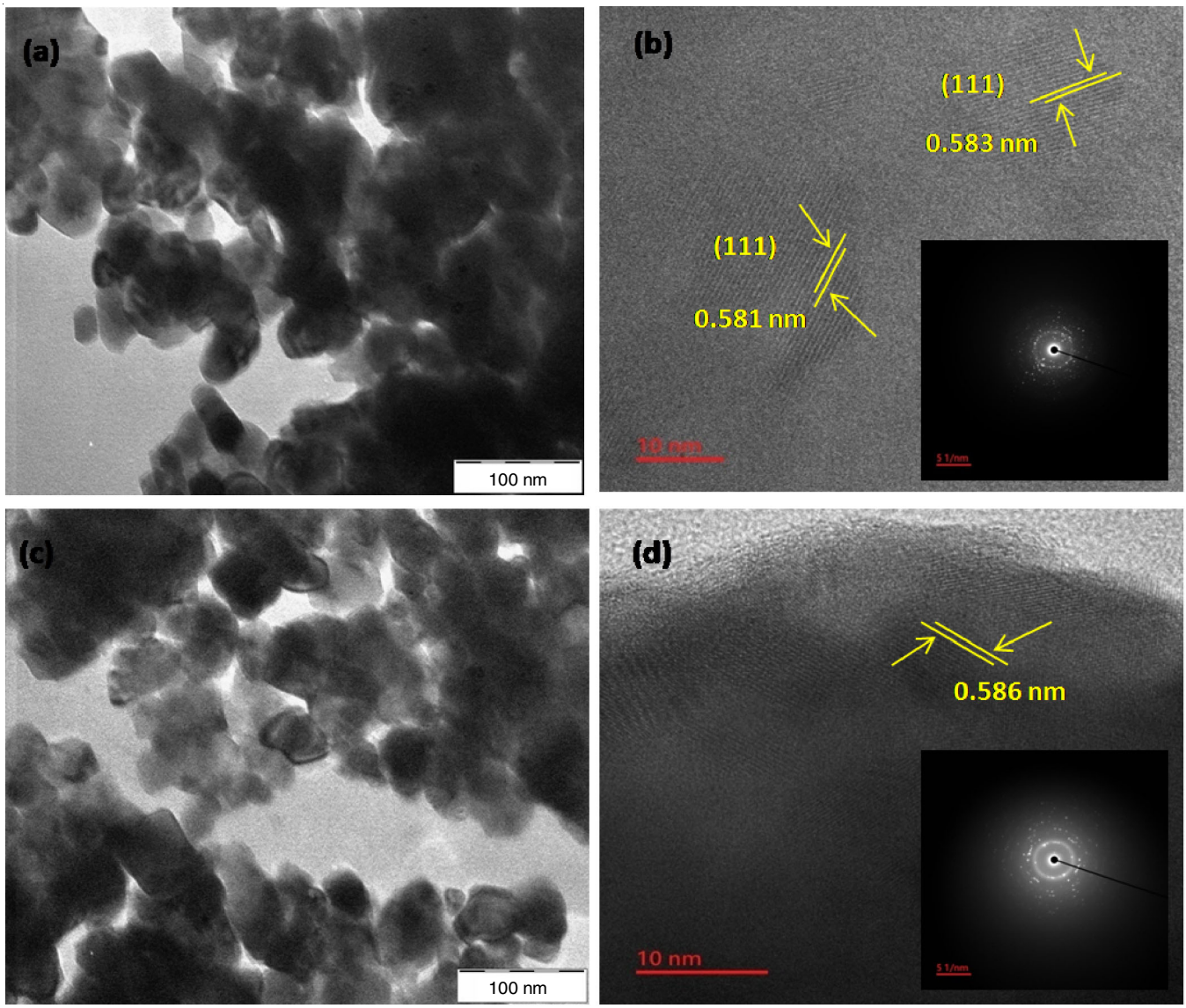

Fig. 5. (a,c) TEM images and (b,d) HRTEM images of KMnTeO and HMnTeO (inset shows the SAED patterns)

nm) surprisingly increased in comparison to parent KMnTeO, indicating that H^+ ions have replaced K^+ ions within the KMnTeO lattice and potentially leading to lattice distortion. In principle, the interplanar spacing of HMnTeO should decrease when H^+ replaces K^+ in the KMnTeO lattice because H^+ has a smaller ionic radius than K^+. However, the interplanar spacing of the (111) plane of HMnTeO exhibited a higher value than that of parent KMnTeO. This phenomenon is attributed due to the substitution of H^+ into the KMnTeO lattice may be in the form of H_3O^+ whose size is larger than the ionic radius of K^+. The SAED pattern of both samples is also provided in the inset of HRTEM images. These patterns indicate several small pots making up diffraction rings, which indicate that a polycrystalline nature characterizes the synthesized samples.

FTIR and Raman studies: FTIR spectra were recorded to characterize the surface functional groups in KMnTeO and HMnTeO samples. The resulting FTIR spectra are shown in Fig. 6a. For defect pyrochlore oxides, the region of interest in FTIR absorption spectra is usually in the range of 1000-400 cm^{-1} due to the bond vibration frequencies of cations in the crystal lattice [21,22]. The FTIR spectrum of parent KMnTeO exhibited two strong and well-defined absorption bands, which are located at 455 and 723 cm^{-1}. These peaks correspond to the stretching vibrations of the Mn-O and Te-O in the MnO_6/TeO_6 octahedral units, respectively. The HMnTeO exhibited additional bands around at 1630 and 3350 cm^{-1}, which can be attributed to O-H stretching and bending vibration modes of surface/lattice waters, respectively [15]. The absence of these bands in the IR spectrum of parent KMnTeO indicates the absence of water molecules. Moreover, that the FT-IR spectrum of HMnTeO exhibited a similar spectrum of KMnTeO, but the peak positions were shifted to a lower wavenumber relative to KMnTeO. This shift may result from substituting protonic species into the KMnTeO lattice. It is well-known that AB_2O_6 type pyrochlore oxides (A, (B′B″) and O occupy 32e, 16c and 48f Wyckoff positions) are likely to give a total of 21 normal modes ($\Gamma = 4F_{2g} + 6F_{1u} + 2A_{2u} + 2E_u + 3F_{2u} + A_{1g} + E_g + 2F_{1g}$). Of these 21 modes, A_{1g}, F_{2g} and E_g modes are Raman active

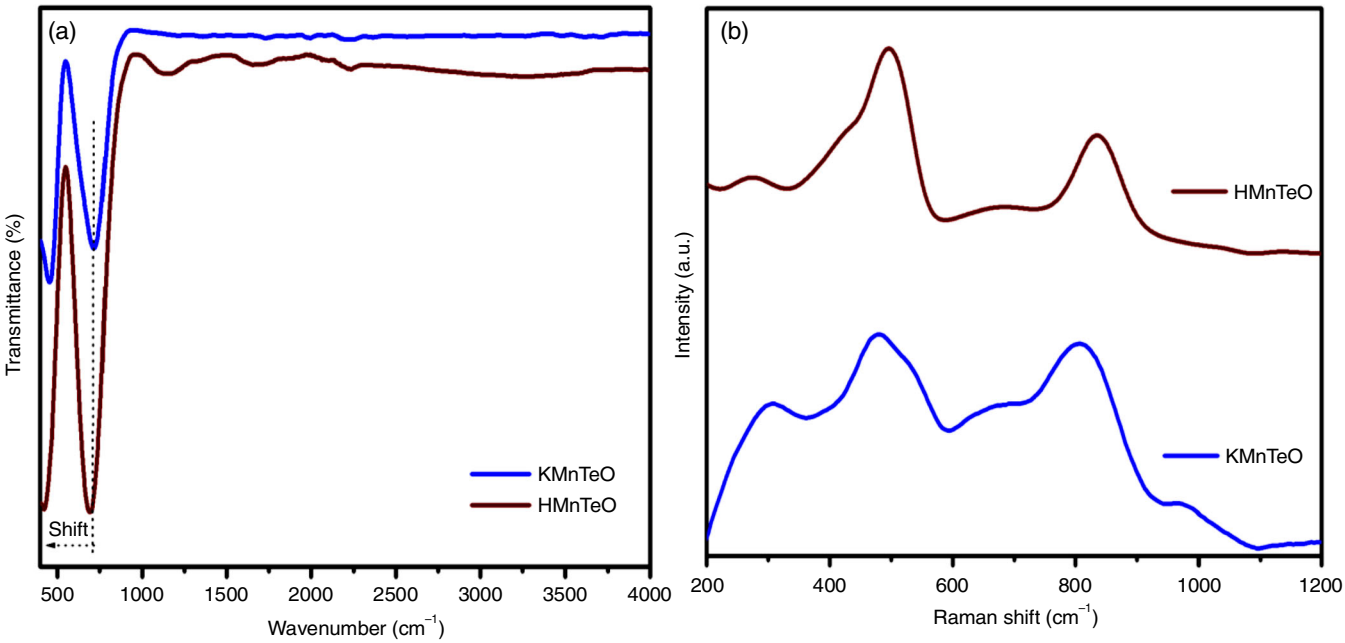

Fig. 6. (a) FT-IR and (b) Raman spectra of KMnTeO and HMnTeO

and F_{1u} modes are IR active [23,24]. The Raman spectra of KMnTeO and HMnTeO are shown in Fig. 6b. The similarity of these Raman spectra with other AB_2O_6-type oxides confirms the formation of KMnTeO in the defect pyrochlore lattice. The slight variation of positions of Raman bands confirms the substitution of K^+ by protonic ions. The Raman spectra of KMnTeO (HMnTeO) exhibits peaks at 305 (280), 498 (414), 672 (677), 810 (830) and 970 (1005) cm^{-1}. The several Raman bands observed is comparable with $CsTaWO_6$ and $RbNbTaO_6$ [25]. The bands observed at 305 (280) and 498 (414) cm^{-1} correspond to E_g, F_{2g} (bending) and A_{1g} Raman active modes [23]. The weak band observed at 672 (677) cm^{-1} may be due to Raman inactive F_{1u} mode [25]. It is observed that both ordered ($A_2B_2O_7$) and defect pyrochlore ($AB'B''O_6$) oxides do not give bands above 700 cm^{-1}. The observed bands at 810 (830) and 970 (1005) cm^{-1} may be due to B′-O and B″-O stretching modes, respectively [25].

Thermal studies: Thermogravimetric analysis (TGA) was carried out to understand the thermal characteristics of synthesized samples and the amount of water entered into HMnTeO. The TGA profiles of both samples were recorded in the temperature range of 100-900 ºC (Fig. 7). The TGA profile of parent KMnTeO shows less than 0.3% weight loss up to 250 ºC, which may be due to adsorbed water at the surface and between 250 and 600 ºC, the weight loss was negligible. The KMnTeO was found to decompose above 650 ºC. The thermogram of HMnTeO, on the other hand, is slightly different compared to the parent KMnTeO. The TGA profile of HMnTeO was characterized by three weight loss regions in the temperature range of 100-600 ºC. It shows a weight loss of ≈ 3% up to 300 ºC and another 2% loss in the 300-650 ºC regions. This weight loss observed up to 600 ºC may be due to adsorbed and lattice water molecules, respectively [26]. Above 650 ºC, continuous weight loss is observed probably due to the volatilization and/or decomposition of HMnTeO.

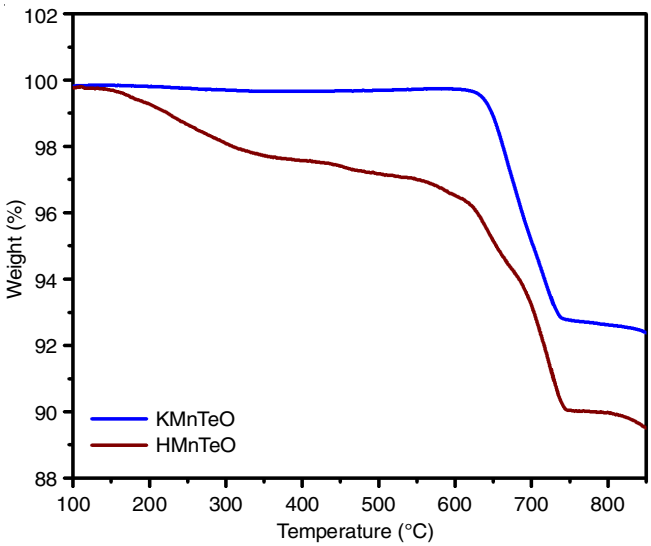

Fig. 7. Thermogravimetric profiles of KMnTeO and HMnTeO

Optical studies: The optical absorbance of the as-prepared samples was investigated using UV-Vis DRS in the 200-800 nm and the obtained data are shown in Fig. 8a. It can be seen that both samples exhibit two absorption peaks that are located at 260 and 395 nm. These peaks are due to the transition from the valence band to the conduction band. Both samples have good absorbance in the visible range, suggesting better photocatalytic degradation capacities under visible light irradiation. The colour of both samples also provided supportive information regarding their absorption in the visible region (Fig. 8a). Notably, the absorbance ability of HMnTeO is slightly higher than that of parent KMnTeO. The higher absorbance can be indicative of the higher photocatalytic activity of the sample. Besides, the bandgap of the material can be obtained from $(\alpha h\nu)^{1/2}$ *vs.* hν graph by extrapolating the linear portion to the *x*-axis (Fig. 8b). However, the larger tailing obtained for these

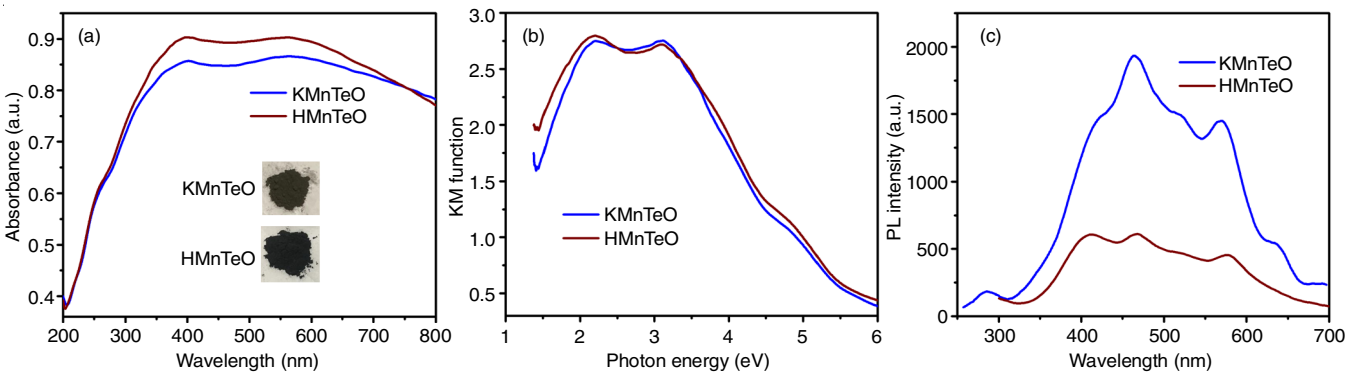

Fig. 8. (a) UV-Vis DRS, (b) Kubelka-Munk function and (c) room-temperature photoluminescence (PL) spectra of KMnTeO and HMnTeO

samples in Kubelka-Munk plots makes it inconvenient to ascertain the exact bandgap values. The separation efficiency of photogenerated electron-hole pairs can be mentioned among the factors affecting the photocatalytic performance of semiconductors [27].

In this work, to investigate the separation efficiency of photo-generated electron-hole pairs, photoluminescence (PL) emission spectra were measured at an excitation wavelength of 240 nm (Fig. 8c). As observed from Fig. 8c, the HMnTeO exhibited a similar PL spectral behaviour with that of parent KMnTeO. However, it is apparent that the intensity of PL emission decreased after the doping of protonic ions. It is widely accepted that PL intensity is an indication of an electron-hole recombination rate; a lower PL intensity reveals slow recombination and, a longer lifetime of electron-hole pairs. Therefore, the doping of protonic ions lowered recombination and promoted the separation of photogenerated electron–hole pairs, which eventually contributed to a higher photocatalytic degradation performance.

XPS studies: XPS was performed to study the chemical composition and oxidation state of the KMnTeO and HMnTeO surface elements. The elemental survey scan of KMnTeO and HMnTeO exhibited featured peaks (KMnTeO: K, Mn, Te and O; HMnTeO: Mn, Te and O except H) confirming the presence of all constituent elements in both samples (Fig. 9). The absence of hydrogen peaks in HMnTeO is due to the low atomic mass of hydrogen. The status of surface elements was further examined by the high-resolution XPS spectra, which were fitted with PeakFit software and the corresponding K 2p, Mn 2p, Te 3d and O 1s core levels are shown in Fig. 10a-d, respectively. The K 2p (Fig. 10a) showed two peaks at 292.6 and 296.5 eV for K $2p_{3/2}$ and K $2p_{1/2}$, respectively. This confirms the existence of K^+ states in KMnTeO [28]. The Mn 2p spectrum (Fig. 10b) showed two peaks located at 641.7 and 653.4 eV for Mn $2p_{3/2}$ and Mn $2p_{1/2}$, respectively, with a binding energy difference (Δ) of 11.6 eV, aligning closely with the literature values. The binding energy values of the Mn 2p core level peaks and the difference (Δ) of the Mn element confirm the presence of Mn^{3+} ions [29]. The Te 3d spectra displayed in Fig. 10c contain two distinct peaks that appeared at 576.7 and 587.2 eV for Te $3d_{5/2}$ and Te $3d_{3/2}$ states, respectively, indicating that validating that Te exists in the form of a hexavalent state (Te^{6+}) [30]. In Fig. 10d, the O 1s core-level spectra in the scanning region of 522-537 eV exhibit an asymmetric feature, indicating more

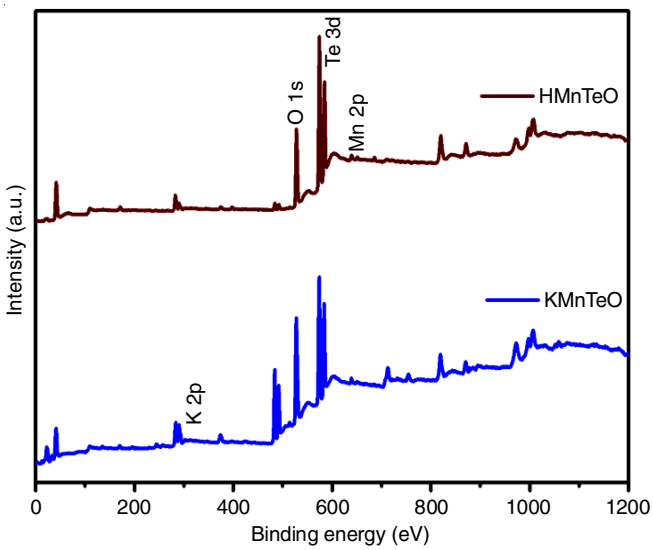

Fig. 9. XPS spectra of KMnTeO and HMnTeO

than one kind of oxygen species in the samples. Therefore, the asymmetric feature can be resolved into two symmetrical peaks with binding energy positions at 529.6 and 531.5 eV. The peak at 530.9 eV can be due to oxygen atoms bonded to Mn/Te ions of the cubic lattice (O_L) and the peak at 532.7 eV can be attributed to surface adsorbed oxygen (O_{SH}) such as hydroxyl groups (OH^-), respectively [31]. Furthermore, we calculated the O_{SH} concentration to be 29.14% and 49.95% for KMnTeO and HMnTeO, respectively. A significant observation is that the O_{SH} concentration of HMnTeO is higher than that of parent KMnTeO, which indicates the higher oxygen adsorption capability of HMnTeO, which improves the hydroxyl radicals. This is beneficial from a photocatalysis point of view since it is anticipated that the hydroxyl radicals are responsible for the dye degradation [17,32]. Therefore, the higher concentration of O_{SH} species over HMnTeO may envisage an enhanced photocatalytic activity. Furthermore, the XPS results also demonstrate that the peaks corresponding to K, Mn and O in HMnTeO slightly shift toward lower binding energies than parent KMnTeO. Such shifting in peaks indicates the substitution of potassium with protonic species.

Photocatalytic studies: Methylene blue dye is well known for its dyeing and medical applications, thus finding numerous ways into the natural ecosystems [33]. A widely adopted adsorption method can only displace the target from water to adsor-

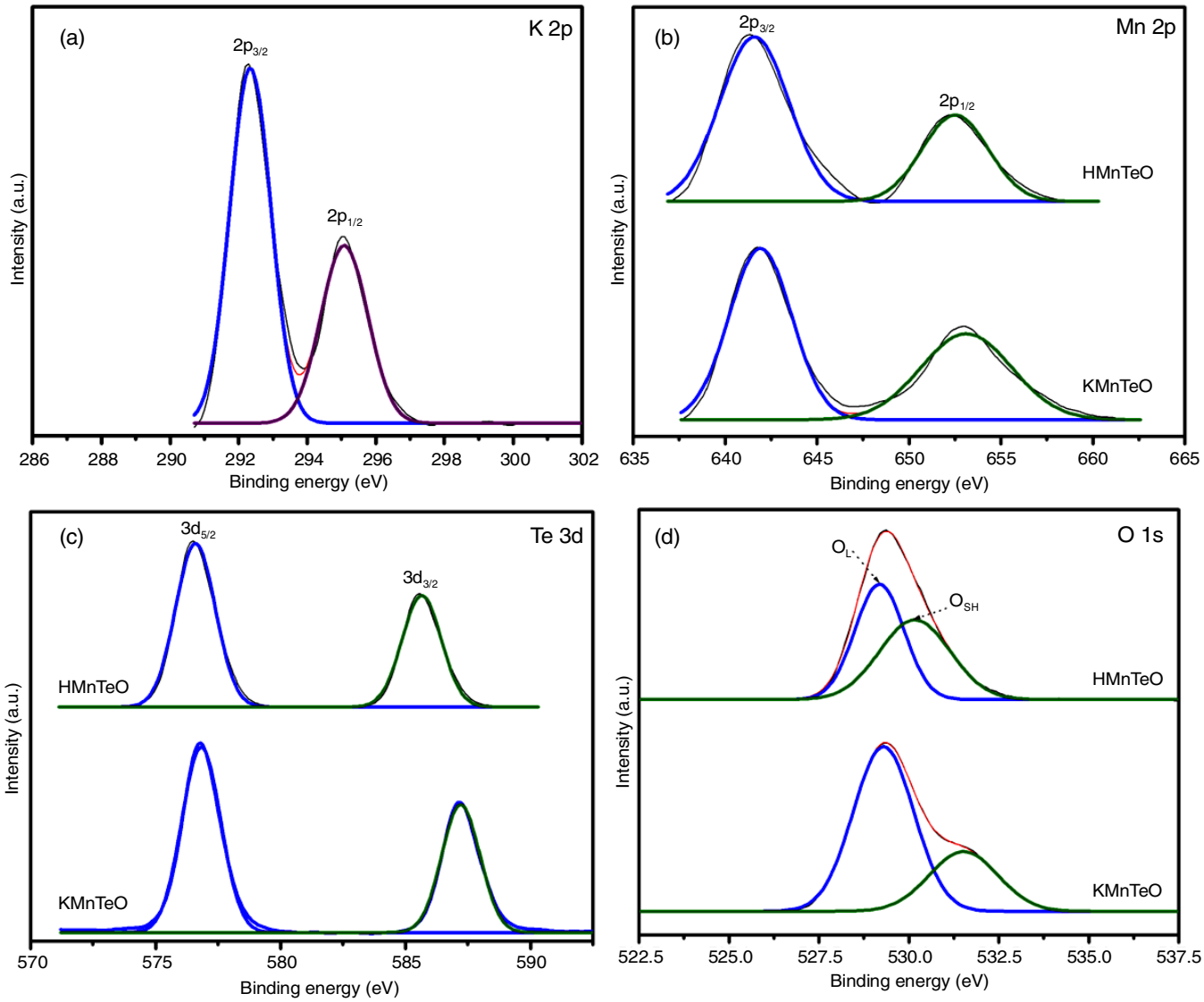

Fig. 10. High-resolution XPS spectra (a) K 2p of KMnTeO, (b) Mn 2p, (c) Te 3d and (d) O 1s of KMnTeO and HMnTeO

bent, not completely abating the dye. In light of which, we have conducted photocatalytic methylene blue degradation studies using the as-prepared photocatalysts to decompose the complex organic structure into simple byproducts. The time-dependent UV-Vis absorption spectral patterns of methylene blue solution over KMnTeO and HMnTeO are shown in Fig. 11a and b, respectively. The methylene blue solution shows two absorption peaks at 615 and 662 nm, which corresponding to the conjugated π-system of methylene blue. The maximum absorbance intensity of the methylene blue solution occurred near 662 nm (λ_{max}); the quite rapid reduction in the intensity of λ_{max} peak with an increase in irradiation time provided proof that methylene blue dye degradation occurred under visible light irradiation over HMnTeO. The C_t/C_0 *vs.* irradiation time plot obtained for photocatalysis evaluation with KMnTeO, HMnTeO and without the usage of photocatalyst (control) is shown in Fig. 11c. As can be observed from Fig. 11c, the photocatalytic degradation of methylene blue dye in the absence of a catalyst was minimal (10%), while that in the presence of photocatalyst has enhanced to more than 93.7% (KMnTeO) and 98.3% (HMnTeO) in 180 min. This suggests that even minimal amounts of photocatalyst (50 mg) can effectively mitigate the methylene blue dye within a short irradiation time. The higher photocatalytic activity of HMnTeO than that of parent KMnTeO is attributed to the higher visible light absorption, effective separation of photogenerated electron-hole pairs and higher surface adsorbed oxygen species concentration. Further, the chemical kinetics of photocatalytic degradation was studied by plotting $\ln(C_0/C_t)$ *vs.* irradiation time, which suggested a pseudo-first-order kinetics (Fig. 11d) as per the Langmuir-Hinshelwood model:

$$\ln\left(\frac{C_o}{C_t}\right) = kt \tag{1}$$

where k is a pseudo-first-order rate constant (min^{-1}), t is the irradiation time (min), C_t is the concentration at time "t" and C_0 is the initial concentration [34]. The apparent rate constants (kapp) of values were 1.67×10^{-2} and 2.07×10^{-2} min^{-1} for parent KMnTeO and HMnTeO, respectively. It is obvious that the photocatalytic degradation rate constant of methylene blue

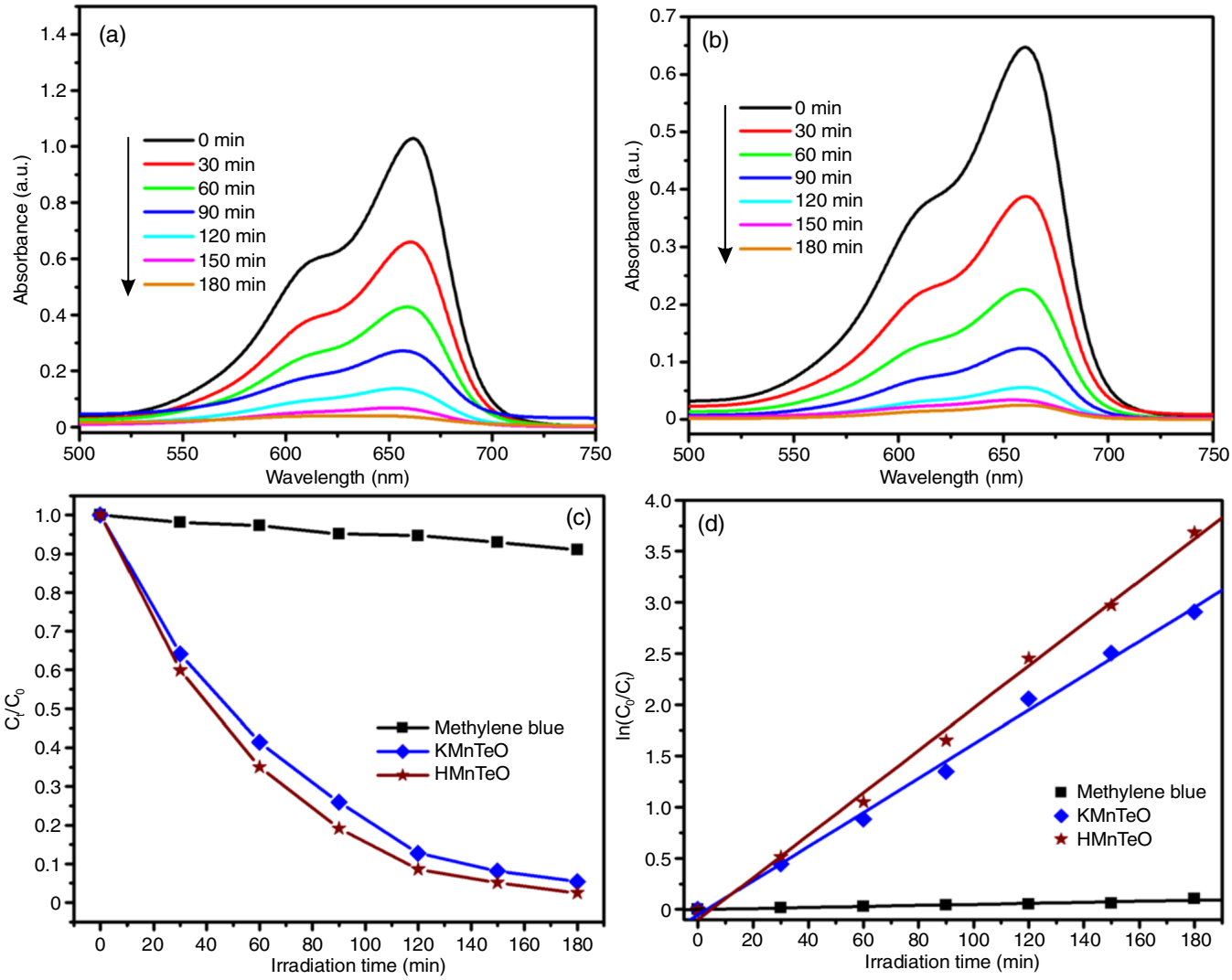

Fig. 11. Exemplified UV-Vis absorbance profiles of methylene blue with irradiation time in presence of (a) KMnTeO, (b) HMnTeO, (c) photocatalytic degradation activity and (d) kinetic plot of photocatalytic degradation methylene blue using blank, KMnTeO and HMnTeO

over HMnTeO is 1.24 times higher than the parent KMnTeO under visible light irradiation.

Radical trapping experiments were carried out to identify which reactive species are more actively driving the methylene blue degradation over HMnTeO. The scavengers employed in this experiment are benzoquinone (BQ, as scavenger of $O_2^{\bullet-}$ radical, 2 mM), isopropanol (IPA, as scavenger of $^{\bullet}OH$ radicals, 2 mM) and ammonium oxalate (AO, as scavenger of h^+, 2 mM). The observed scavengers effect on the photocatalytic degradation of methylene blue is shown in Fig. 12a, which clearly indicated that the photocatalytic degradation efficiency is immensely affected by the addition of IPA, attaining a degradation efficiency of 29.3% as compared to without scavengers (98.3%). Moreover, with the addition of BQ, the degradation of methylene blue is retarded to a moderate extent. However, no significant change in the degradation of methylene blue is observed upon the addition of AO. These observations validate that the primary species involved in the photocatalytic degradation of methylene blue are $^{\bullet}OH$ and $O_2^{\bullet-}$ radicals, with the $^{\bullet}OH$ radicals serving as the dominant oxidizing agent. Moreover, the sole contribution of $^{\bullet}OH$ radicals was further confirmed by the terephthalic acid probe molecule using PL analysis (Fig. 12b). It could be seen that the PL emission intensity was very weak and almost negligible under dark conditions and then the PL intensity (HTA; due to the formation of $^{\bullet}OH$) gradually increased with increasing irradiation time, as evidenced by the PL signal observed at 425 nm. Additionally, the comparative PL spectra of HTA over both samples after irradiation of 90 min are shown in Fig. 13. It is evident that HMnTeO has a larger rate of $^{\bullet}OH$ radical generation on its surface than parent KMnTeO, which results in enhanced photocatalytic activity.

Stability and reusability studies: It is indispensable to evaluate the stability and reusability of the prepared catalyst since it could significantly reduce the overall expenditure for the wastewater treatment processes and avert secondary pollution. Therefore, the reusability of the HMnTeO sample was explored for five successive cycles; the results are given in Fig. 12c. After the completion of every cycle, the photocatalyst was centrifuged, filtered and washed repeatedly with deionized water and then dried at 80 °C overnight before being reintroduced

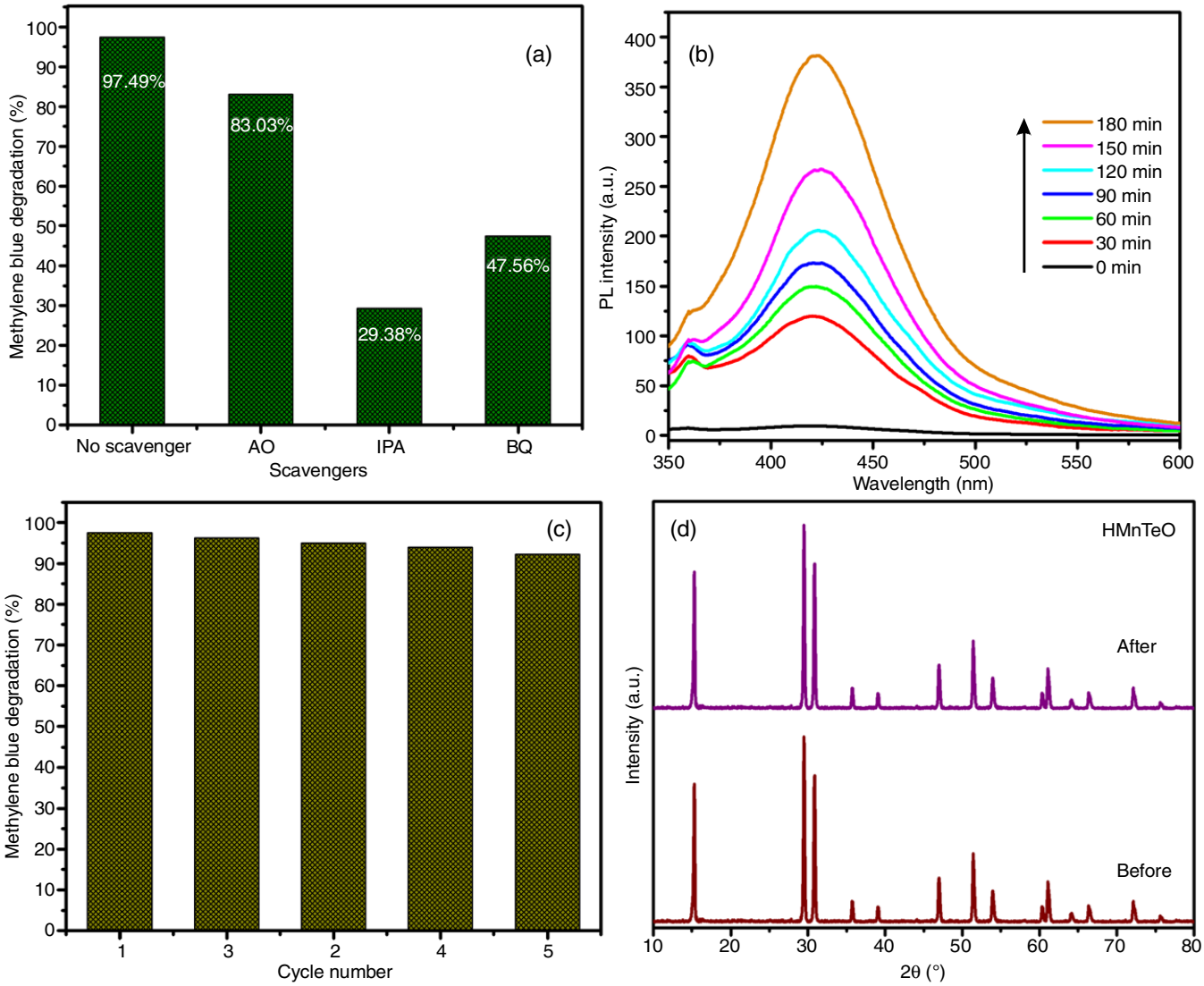

Fig. 12. (a) Reactive oxygen species trapping of HMnTeO using IPA, BQ and AO under visible light irradiation, (b) •OH radicals trapping PL using HMnTeO with TA solution under visible-light irradiation (λ_{ex} = 325 nm), (c) photocatalytic recyclability up to five cycles and (d) powder XRD patterns of HMnTeO before and after fifth cycle

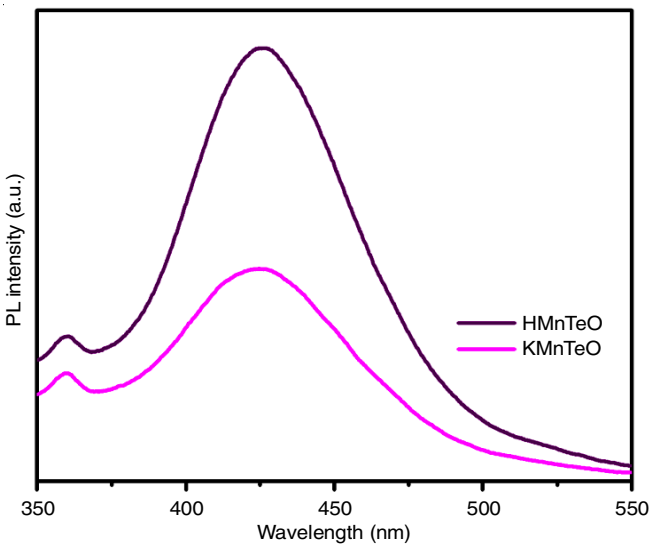

Fig. 13. A comparison of •OH trapping PL spectra of KMnTeO and HMnTeO for an irradiation of 90 min

for the next experimental cycle. As shown in Fig. 12c, the photocatalytic degradation efficiency of methylene blue dye was slightly decreased after five consecutive cycles, so it can be considered as cost-effective photocatalyst. Fig. 12d shows the XRD patterns of the HMnTeO before and after photocatalytic degradation of methylene blue dye. It can be seen that there are no observable structural differences in the sample before and after the degradation, demonstrating that the phase and structure of HMnTeO are stable during the photocatalytic activity, thus confirming its high stability and sustainability.

Mechanism: The following equations can summarize a as a possible mechanistic rationale for HMnTeO-assisted photocatalytic degradation of methylene blue dye under visible light. In line with the UV-Vis DRS results, the HMnTeO sample exhibits a strong visible light absorption. As visible light falls on HMnTeO, electron–hole pairs are generated on the HMnTeO surface. This causes the excitation of electrons from the valence band (VB) to the conduction band (CB), leading to the gener-

ation of electron and hole in the VB and CB, respectively. The photogenerated electrons in the CB react with oxygen (O_2) molecules, which boost the production of $O_2^{\bullet-}$ radicals. Furthermore, photogenerated holes that have strong oxidability can react with the adsorbed water/hydroxyl groups and produce highly oxidative $^{-\bullet}OH$ radicals. Later, the formed hydroxyl and superoxide radicals react with absorbed methylene blue on the HMnTeO surface, which leads to the degradation process of methylene blue. However, the drastic decrease in photocatalytic degradation rate in the presence of an $^{\bullet}OH$ scavenger (IPA) further confirmed that hydroxyl radicals primarily mediated the methylene blue degradation over HMnTeO.

$$HMnTeO + h\nu \rightarrow e^- (CB) + h^+ (VB) \quad (2)$$

$$e^- (CB) + O_2 \rightarrow O_2^{\bullet-} \quad (3)$$

$$h^+ (VB) + H_2O (ads) \rightarrow {}^{\bullet}OH + H^+ \quad (4)$$

$$\text{Reactive species } ({}^{\bullet}OH \text{ and } O_2^{\bullet-}) + MB \rightarrow CO_2 + H_2O \quad (5)$$

Removal of Pb^{2+} using ion-exchange over KMnTeO: Defect pyrochlore oxides of type AB_2O_6 are known to exchange specific metal ions in aqueous solutions [35,36]. An attempt was made to remove the Pb^{2+} ions from $Pb(NO_3)_2$ solution by ion-exchange process with parent KMnTeO. The precipitate (KPbMnTeO) obtained when KMnTeO was added to 0.011M $Pb(NO_3)_2$ solution was subjected to XRD and EDX analyses. The powder X-ray diffraction (XRD) pattern of KPbMnTeO is similar to that of the parent compound KMnTeO, demonstrating that the resultant KPbMnTeO has maintained the same structure even after the exchange of K^+ with Pb^{2+} ions (Fig. 14a). The morphology of KPbMnTeO was similar to that of parent KMnTeO as shown in Fig. 14b. The EDX analysis of KPbMnTeO confirmed that K^+ ions are replaced by Pb^{2+} ions, as depicted in Fig. 14c. Furthermore, the results show that about 21.72% of K^+ ions were replaced by Pb^{2+} ions. The XPS analysis was also used to confirm the exchange of Pb^{2+} ions on the surface of KMnTeO. The survey scan spectrum (Fig. 14d) shows the evident peaks that are marked with their corresponding energy levels. It identifies the presence of K, Mn, Te, O and Pb elements, which is consistent with the chemical composition of KPbMnTeO. Fig. 14e shows the high-resolution XPS spectra for the Pb 4f, the curve-fitting shows two peaks at 135.8 and 140.6 eV corresponding to elemental Pb $4f_{7/2}$ and Pb $4f_{5/2}$ states, respectively, which belongs to the characteristics of Pb^{2+} ions in KPbMnTeO [37]. Therefore, Pb^{2+}, a heavy metal ion, can be eliminated from aqueous solutions using the parent KMnTeO.

Conductivity studies: As mentioned in the introduction, the "A" ions located in the tunnels are free to move and responsible for ionic conduction. The magnitude of the conductivity depends on the ionic size of the cation "A". It is reported that hydrated defect pyrochlore type oxides of composition $A(BB')O_6 \cdot xH_2O$ are known to exhibit ionic conductivity in the range $6.3 \times 10^{-3} - 5.2 \times 10^{-5}$ S cm^{-1} at 573 K [7,38]. Replacement of K^+ with H_3O^+ ion may exhibit relatively high conductivity due to the small size and high mobility of the proton species [39-41]. The DC conductivity of KMnTeO and HMnTeO samples was also investigated. It is observed that at any temperature the DC conductivity of HMnTeO is higher than that of KMnTeO. Both samples exhibit an increase in DC conductivity with temperature in the range 336-636 K because of the thermal activation of conducting species (Fig. 15). The relationship between conductivity and temperature can be explained by the Arrhenius equation:

$$\sigma_{dc} T = \sigma_0 \exp\left(\frac{E_a}{k_B T}\right) \quad (6)$$

where E_a is the activation energy for conduction, σ_0 is pre-exponential factor and k_B is the Boltzmann constant. Both E_a and σ_0 are considered temperature-independent. The experimental data was fitted to the above equation and the obtained E_a is displayed in Table-2 along with the conductivity values at 636 K. These values are comparable with those obtained for similar compositions [19,42]. It was reported that $BB'O_6$ network and polarizability of B-O-B′ linkages favour the movement of the ions through the tunnels, leading to better ionic conductivity [8,43].

TABLE-2
DC CONDUCTIVITY (AT 636 K) AND ACTIVATION ENERGIES OF KMnTeO AND HMnTeO

Parameter	KMnTeO	HMnTeO
DC conductivity (S cm$^{?1}$)	$3.16 \times 10^{?5}$	$3.6 \times 10^{?4}$
E_a (eV)	0.2698	0.3031

Conclusion

In summary, we have successfully synthesized $KMn_{0.33}Te_{1.67}O_6$ (KMnTeO) and its proton-exchanged analogue (HMnTeO) by solid-state and facile ion-exchange methods, respectively. The proposed synthesis methods yield samples with defect pyrochlore structures possessed with excellent phase purity. Their structure, morphology, optical and photocatalytic properties were characterized in detail. The XRD analysis showed that the KMnTeO and HMnTeO were crystallized in a cubic lattice with the $Fd\bar{3}m$ space group. The SEM images of KMnTeO and HMnTeO show that the resulting particles have a polyhedral shape. The UV-Vis DRS results demonstrated that both samples observed a pronounced absorption in the visible region and the photoluminescence (PL) spectra confirmed that the recombination rate of photogenerated electron-hole pairs can be inhibited greatly in the presence of HMnTeO, increasing photon efficiency. The photocatalytic degradation of methylene blue dye was chosen as the probe reaction and both samples exhibit good photocatalytic activity under visible light irradiation. HMnTeO shows the highest photocatalytic activity than that of parent KMnTeO under investigation. The relatively higher photocatalytic activity of HMnTeO was attributed to the increase in the visible light absorption range and reduced charge recombination of the photogenerated electron-hole pairs. The photocatalytic activity was also found to correlate with the concentration of $^{\bullet}OH$ radicals and found to be higher for HMnTeO, which is supported by the terephthalic acid probe experiment. The active species trapping experiments demonstrated that the $^{\bullet}OH$ radicals are the main active species in the HMnTeO and superoxide radicals also play a key role in the photocatalytic degradation of methylene blue dye. The HMnTeO

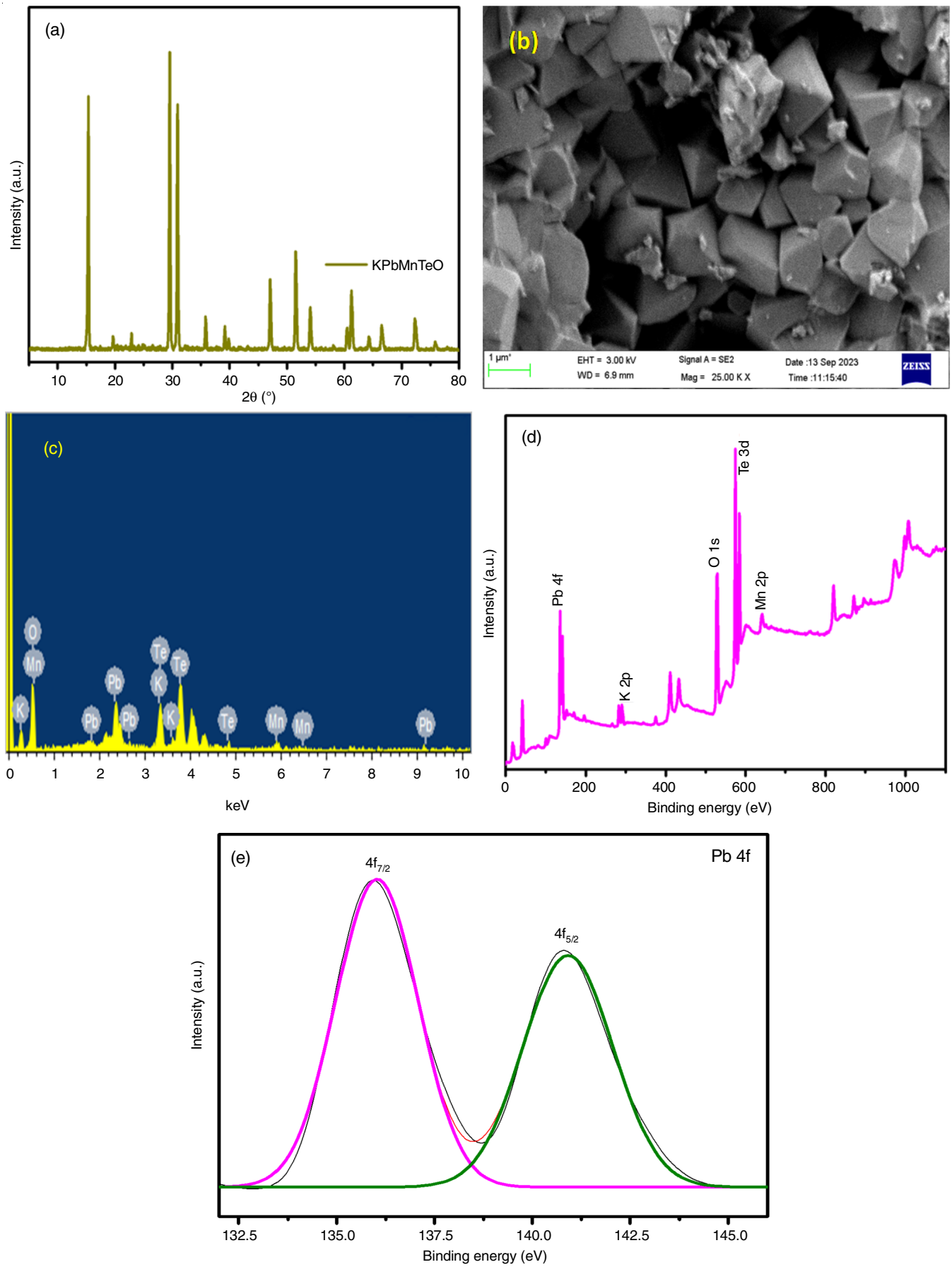

Fig. 14. (a) Powder XRD, (b) FESEM, (c) EDX, (d) survey scan and (e) high-resolution XPS spectra of Pb 4f of KPbMnTeO

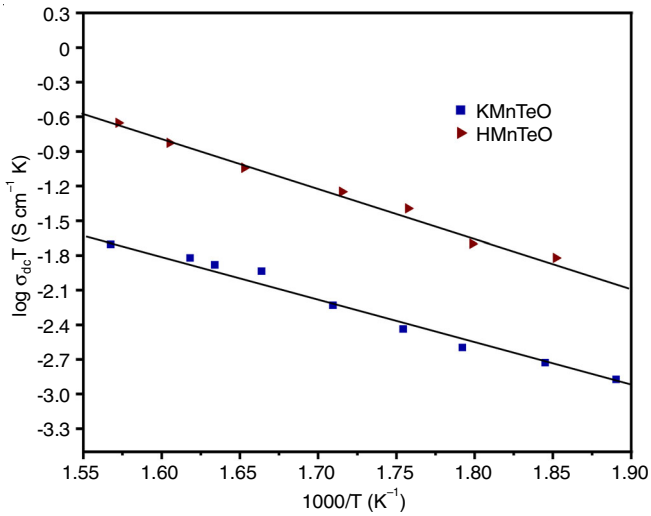

Fig. 15. Arrhenius plots of DC conductivity (log σ) as function of reciprocal temperature over KMnTeO and HMnTeO

retains excellent photocatalytic activity even after five cycles of use, demonstrating its promising cycling ability. In addition, the parent KMnTeO can used be to remove of heavy metal ion, Pb^{2+}, from aqueous solutions. The DC conductivity was also investigated as a function of temperature, which shows the conductivity of HMnTeO is higher than that of parent KMnTeO.

ACKNOWLEDGEMENTS

One of the authers, MV thanks CSIR, New Delhi, for the award of Emeritus Scientist (Grant No. 21(1115)/20/EMR-II).

CONFLICT OF INTEREST

The authors declare that there is no conflict of interests regarding the publication of this article.

REFERENCES

1. R. Atchudan, T.N.J.I. Edison, S. Perumal, D. Karthikeyan and Y.R. Lee, *J. Photochem. Photobiol. Chem.*, **333**, 92 (2017); https://doi.org/10.1016/j.jphotochem.2016.10.021
2. V. Innocenzi, M. Prisciandaro, M. Centofanti and F. Veglio, *J. Environ. Chem. Eng.*, **7**, 103171 (2019); https://doi.org/10.1016/j.jece.2019.103171
3. Y. Li, H. Zhao and M. Yang, *J. Colloid Interface Sci.*, **508**, 500 (2017); https://doi.org/10.1016/j.jcis.2017.08.076
4. Y. Liu, S. Shen, J. Zhang, W. Zhong and X. Huang, *Appl. Surf. Sci.*, **478**, 762 (2019); https://doi.org/10.1016/j.apsusc.2019.02.010
5. R.J.E. Martins, R. Pardo and R.A.R. Boaventura, *Water Res.*, **38**, 693 (2004); https://doi.org/10.1016/j.watres.2003.10.013
6. A. Sarý and M. Tuzen, *J. Hazard. Mater.*, **164**, 1004 (2009); https://doi.org/10.1016/j.jhazmat.2008.09.002
7. M.A. Subramanian, G. Aravamudan and G.V. Subba Rao, *Prog. Solid State Chem.*, **15**, 55 (1983); https://doi.org/10.1016/0079-6786(83)90001-8
8. J.B. Goodenough, H.Y.-P. Hong and J.A. Kafalas, *Mater. Res. Bull.*, **11**, 203 (1976); https://doi.org/10.1016/0025-5408(76)90077-5
9. D.R. Modeshia and R.I. Walton, *Chem. Soc. Rev.*, **39**, 4303 (2010); https://doi.org/10.1039/b904702f
10. R.R. Jitta, R. Gundeboina, N.K. Veldurthi, R. Guje and V. Muga, *J. Chem. Technol. Biotechnol.*, **90**, 1937 (2015); https://doi.org/10.1002/jctb.4745
11. M. Weiss, B. Wirth and R. Marschall, *Inorg. Chem.*, **59**, 8387 (2020); https://doi.org/10.1021/acs.inorgchem.0c00811
12. P. Venkataswamy, C. Sudhakar Reddy, R. Gundeboina, G. Sadanandam, N.K. Veldurthi and M. Vithal, *Electron. Mater. Lett.*, **14**, 446 (2018); https://doi.org/10.1007/s13391-018-0055-9
13. G. Ravinder, P. Shrujana, V.N. Kumar, G. Ravi, K.N. Rao and M. Vithal, *Chem. Pap.*, **69**, 269 (2015); https://doi.org/10.1515/chempap-2015-0013
14. R. Guje, G. Ravi, S. Palla, K.N. Rao and M. Vithal, *Mater. Sci. Eng. B*, **198**, 1 (2015); https://doi.org/10.1016/j.mseb.2015.03.010
15. R. Guje, R. Gundeboina, J.R. Reddy, N.K. Veldurthi, S. Kurra and M. Vithal, *Photochem. Photobiol.*, **92**, 223 (2016); https://doi.org/10.1111/php.12559
16. A. Siddikha, B. Sathyanarayana, V. Muga and M. Abdul Mujeeb, *Chem. Inorg. Mater.*, **3**, 100053 (2024); https://doi.org/10.1016/j.cinorg.2024.100053
17. H.A. Kiwaan, T.M. Atwee, E.A. Azab and A.A. El-Bindary, *J. Chin. Chem. Soc.*, **66**, 89 (2019); https://doi.org/10.1002/jccs.201800092
18. G. Ravi, N.K. Veldurthi, S. Palla, R. Velchuri, S. Pola, J.R. Reddy and M. Vithal, *Photochem. Photobiol.*, **89**, 824 (2013); https://doi.org/10.1111/php.12079
19. G. Ravinder, J.R. Reddy, C.S. Reddy, K. Sreenu, G. Ravi and M. Vithal, *Adv. Mater. Lett.*, **7**, 536 (2016); https://doi.org/10.5185/amlett.2016.6073
20. B. Darriet, M. Rat, J. Galy and P. Hagenmuller, *Mater. Res. Bull.*, **6**, 1305 (1971); https://doi.org/10.1016/0025-5408(71)90129-2
21. F.E. López-Suárez, A. Bueno-López, M.J. Illán-Gómez and J. Trawczynski, *Appl. Catal. A Gen.*, **485**, 214 (2014); https://doi.org/10.1016/j.apcata.2014.07.037
22. M.H. Esfahani, H. Naji, C.A. Marjerrison, J. Greedan and M. Behzad, *Ceram. Int.*, **48**, 13651 (2022); https://doi.org/10.1016/j.ceramint.2022.01.244
23. M. Maczka, A.V. Knyazev, N.Y. Kuznetsova, M. Ptak and L. Macalik, *J. Raman Spectrosc.*, **42**, 529 (2011); https://doi.org/10.1002/jrs.2735
24. A.V. Knyazev, M. Maczka and N.Y. Kuznetsova, *Thermochim. Acta*, **506**, 20 (2010); https://doi.org/10.1016/j.tca.2010.04.009
25. M. Maczka, A.V. Knyazev, A. Majchrowski, J. Hanuza and S. Kojima, *J. Phys. Condens. Matter*, **24**, 195902 (2012); https://doi.org/10.1088/0953-8984/24/19/195902
26. K. Ozawa, J. Wang, J. Ye, Y. Sakka and M. Amano, *Chem. Mater.*, **15**, 928 (2003); https://doi.org/10.1021/cm020990i
27. M. Humayun, Z. Zheng, Q. Fu and W. Luo, *Environ. Sci. Pollut. Res. Int.*, **26**, 17696 (2019); https://doi.org/10.1007/s11356-019-05079-0
28. R. Angineni, P. Venkataswamy, K. Ramaswamy, S. Raj, N.K. Veldurthi and M. Vithal, *Polyhedron*, **214**, 115620 (2022); https://doi.org/10.1016/j.poly.2021.115620
29. S. Baek, Y. Ghaffari and J. Bae, *Catalysts*, **12**, 1045 (2022); https://doi.org/10.3390/catal12091045
30. M. Sathiya, K. Ramesha, G. Rousse, D. Foix, D. Gonbeau, K. Guruprakash, A.S. Prakash, M.L. Doublet and J.-M. Tarascon, *Chem. Commun.*, **49**, 11376 (2013); https://doi.org/10.1039/c3cc46842a
31. S. Balu, S. Velmurugan, S. Palanisamy, S.-W. Chen, V. Velusamy, T.C.K. Yang and E.-S.I. El-Shafey, *J. Taiwan Inst. Chem. Eng.*, **99**, 258 (2019); https://doi.org/10.1016/j.jtice.2019.03.011
32. A.M. Soliman, M. Khalil and I.M. Ali, *J. Water Process Eng.*, **41**, 102086 (2021); https://doi.org/10.1016/j.jwpe.2021.102086
33. V. Jayaraman, C. Ayappan, B. Palanivel and A. Mani, *RSC Adv.*, **10**, 8880 (2020); https://doi.org/10.1039/D0RA00644K
34. U. Farooq, J. Ahmed, S.M. Alshehri and T. Ahmad, *ACS Omega*, **4**, 19408 (2019); https://doi.org/10.1021/acsomega.9b02830

35. M. Abe and T. Itoh, *J. Inorg. Nucl. Chem.*, **42**, 1641 (1980); https://doi.org/10.1016/0022-1902(80)80330-7
36. T. Moller, A. Clearfield and R. Harjula, *Micropor. Mesopor. Mater.*, **54**, 187 (2002); https://doi.org/10.1016/S1387-1811(02)00320-7
37. U.O. Bhagwat, J.J. Wu, A.M. Asiri and S. Anandan, *ChemistrySelect*, **3**, 11851 (2018); https://doi.org/10.1002/slct.201802303
38. J. Grins, M. Nygren and T. Wallin, *Mater. Res. Bull.*, **15**, 53 (1980); https://doi.org/10.1016/0025-5408(80)90159-2
39. G. Mangamma and K. Shahi, *Solid State Ion.*, **76**, 337 (1995); https://doi.org/10.1016/0167-2738(94)00302-9
40. M. Riviere, J.L. Fourquet, J. Grins and M. Nygren, *Mater. Res. Bull.*, **23**, 965 (1988); https://doi.org/10.1016/0025-5408(88)90051-7
41. N. Binesh, V. Bhat and S.V. Bhat, *Solid State Ion.*, **86-88**, 665 (1996); https://doi.org/10.1016/0167-2738(96)00232-9
42. M. Srinivas, G. Ravi, P.V. Kumar, C.S. Reddy, K. Sreenu, G. Ravinder and M. Vithal, *Indian J. Chem.*, **56A**, 270 (2017).
43. A.W. Sleight, J.E. Gulley and T. Berzins, *Adv. Chem. Ser.*, **163**, 195 (1977); https://doi.org/10.1021/ba-1977-0163.ch011